Environmental Science Nano

ROYAL SOCIETY OF CHEMISTRY

PAPER

View Article Online
View Journal | View Issue

Cite this: *Environ. Sci.: Nano*, 2023, **10**, 3156

Porous calcium copper titanate electrodes for paracetamol degradation by electro-oxidation *via* CuO-induced peroxymonosulfate activation†

Elissa Makhoul,[ab] Fida Tanos,[ac] Maged F. Bekheet,[d] Wiebke Riedel,[e] Eddy Petit,[a] Roman Viter,[fg] Iryna Tepliakova,[f] Arunas Ramanavicius,[h] Antonio Razzouk,[c] Geoffroy Lesage,[a] Marc Cretin,[a] Madona Boulos,[b] David Cornu[a] and Mikhael Bechelany *[ai]

Some drugs cannot be efficiently eliminated using routine wastewater treatments and therefore are considered persistent organic pollutants (POPs). POPs can be removed using advanced oxidation processes. Among these processes, the combination of electrocatalysis and a sulfate-based advanced oxidation process *via* peroxymonosulfate (PMS) activation is an attractive approach due to its high efficiency, low energy consumption and non-selective attack. It is well known that the type of anode strongly affects the electrocatalysis performance for water treatment. Here, we evaluated perovskites as electrode material due to their unique structural properties and high chemical stability. We fabricated porous anodes of calcium copper titanate ($CaCu_3Ti_4O_{12}$; CCTO) with different percentages (20%, 30% and 40%) of polymethyl methacrylate (PMMA) by ball-milling. The samples that included PMMA displayed 50% porosity and pores were homogenously distributed. Morphological measurements show the presence of grain structures and grain boundaries containing CCTO and CuO phases, respectively. CCTO with 30 wt% PMMA (CCTO-30) exhibited the highest CuO phase amount, defect percentage and oxidation–reduction peak, and the smallest resistance. We used the obtained CCTO nanocomposites as anodes in a beaker (210 mL) with PMS (0.5 mM) to treat 10 ppm paracetamol in 50 mM sodium sulfate. After 90 minutes, paracetamol was completely decomposed using CCTO-30 due to PMS activation by a copper catalytic cycle (Cu^{2+}/Cu^{1+} and Cu^{2+}/Cu^{3+}) to generate $^{\bullet}SO_4^-$ radicals and Cu^{3+} non-radicals that are selective for its removal.

Received 20th May 2023,
Accepted 16th September 2023

DOI: 10.1039/d3en00317e

rsc.li/es-nano

Environmental significance

Water pollution, particularly from pharmaceuticals, poses significant risks to human health and ecosystems. Eliminating these pollutants at low concentrations is highly challenging. To address this issue, it is vital to develop purification systems that can effectively remove trace compounds. Advanced oxidation processes, such as electrocatalysis combined with peroxymonosulfate activation, have shown promise in this regard. These processes offer efficiency, cost-effectiveness, and environmental friendliness. However, the search for highly active catalysts for anodic oxidation remains ongoing. Calcium copper titanate, an electroceramic composite known as Ti-based perovskite, is a potential catalyst due to its unique structure containing both copper oxide and titanium dioxide phases. This composite could play a vital role in addressing water pollution challenges.

[a] *Institut Européen des Membranes, IEM, UMR 5635, Univ Montpellier, ENSCM, Centre National de la Recherche Scientifique (CNRS), Place Eugène Bataillon, 34095 Montpellier, France.*
E-mail: mikhael.bechelany@umontpellier.fr
[b] *Laboratoire de Chimie Physique des Matériaux (LCPM/PR2N), EDST, Université Libanaise, Faculté des Sciences II, Département de Chimie, Fanar, Lebanon*
[c] *Laboratoire d'Analyses ChimiquesLAC—Lebanese University, Faculty of SciencesJdeidet, 90656, Lebanon*
[d] *Technische Universität Berlin, Faculty III Process Sciences, Institute of Materials Science and Technology, Chair of Advanced Ceramic Materials, Straße des 17. Juni 135, 10623 Berlin, Germany*
[e] *Freie Universität Berlin, Institut für Chemie und Biochemie, Arnimallee 22, 14195 Berlin, Germany*
[f] *Institut of Atomic Physics and Spectroscopy, University of Latvia, Rainis Blvd., LV-1586 Riga, Latvia*
[g] *Center for Collective Use of Scientific Equipment, Sumy State University, Sanatornaya Str. 31, 40018 Sumy, Ukraine*
[h] *Department of Physical Chemistry, Faculty of Chemistry and Geosciences, Institute of Chemistry, Vilnius University, Vilnius, Lithuania*
[i] *Gulf University for Science and Technology, GUST, Kuwait*

† Electronic supplementary information (ESI) available. See DOI: **https://doi.org/10.1039/d3en00317e**

1. Introduction

Persistent organic pollutants (POPs) in water are becoming a major threat worldwide. Organic micropollutants are found in water at very low concentrations (μg L^{-1}–ng L^{-1}) but can have harmful effects on aquatic life and human health. POPs include many different organic compounds (*e.g.* drugs, pesticides/herbicides, and chemicals, such as flame retardants and plasticizers) that are used in everyday life. In particular, anti-inflammatories, lipid regulators, antibiotics, and analgesics are drugs used for the treatment, diagnosis and prevention of diseases and also to modify organic processes.[1–3] These substances are released into the environment mainly through the wastewater of pharmaceutical production facilities, hospitals, and human activities. Due to their stability and persistence in water, these pollutants adversely affect human health and ecosystems.[4,5] For instance, paracetamol, also known as acetaminophen, is a pain-relieving compound commonly consumed worldwide.[2] In aquatic ecosystems, paracetamol is harmful even at low concentrations.[6–9] Therefore, to prevent their potential toxicity, water recycling techniques must ensure adequate water decontamination by removing all drugs and their metabolites. However, conventional wastewater treatment plants only partially remove pharmaceutical contaminants and pose additional problems, including their need of chemical reagents and the formation of by-products or of sludge that is difficult to treat. As a result, many pollutants end up in the environment.[10–12] Among the alternative and more environmentally friendly methods, advanced oxidation processes (AOPs) are considered one of the most promising ways to effectively remove several contaminants by oxidizing organic pollutants into harmless compounds.[13–17] These methods allow the *in situ* generation of hydroxyl radicals that act as non-selective oxidizing agents to destroy non-biodegradable organic molecules in wastewater.[4,6,18–20] These AOPs include catalytic ozonation procedures, sulfate-based AOPs, and treatment with ultrasound, electro-catalytic oxidation, and photocatalysis.[12,21–24] Electrocatalytic oxidation has been extensively studied for wastewater treatment due to its simplicity, capacity to mineralize pollutants without producing secondary pollution, and high oxidation rates by losing electrons at the anode or by oxidizing reactive species, leading to the organic pollutant transformation into CO_2 and H_2O.[25–28] Direct anodic oxidation occurs at the electrode surface by electron transfer. Conversely, in indirect oxidation, first reactive oxygen species are electrochemically formed, and then, they efficiently oxidize organic molecules to produce small biodegradable organic molecules.[29,30] Electrochemical oxidation is influenced by many different variables, such as the applied electrolyte, pH, delivered power, and contaminant type(s) and concentration(s). The choice of anode also strongly affects the electrocatalytic degradation effectiveness.[31–34]

For electro-oxidation, different electrode types can be used (*e.g.* boron-doped diamond, graphite, tin and ruthenium oxide) with different electron transfer ability and number of $^{\bullet}OH$ radicals formed.[35] However, simple single-metal oxides often display low conductivity and limited application in anodic oxidation.[36] Perovskite oxides (ABO_3) are multi-metal oxides that have been thoroughly investigated as a suitable class of electrocatalytic materials due to their unique structure and composition. Perovskite oxides are particularly popular in electrocatalysis due to their (1) low-cost and simple synthesis techniques with excellent stoichiometric control, repeatability, and homogeneity and (2) high capacity to accommodate a wide variety of substituting and doping elements to regulate their properties.[37] For instance, Ma *et al.* synthesized a spinel $Cu_xCo_{1-x}Mn_2O_4$ anode for the electrocatalytic degradation of tetracycline hydrochloride. After 120 minutes, the removal efficiency reached 91.3% with good stability after five cycles of anode reuse. These results can be attributed to the multi-metal oxides present in $Cu_xCo_{1-x}Mn_2O_4$ perovskite that offer high electrocatalytic activity to enhance electron transfer. This leads to the generation of radicals that react with and remove organic pollutants.[37]

$CaCu_3Ti_4O_{12}$ (CCTO) is a cubic ($AA'BO_3$) double-perovskite with Ca^{2+} and Cu^{2+} organized on the A and A′ sites, and with Ti^{4+} arranged on the B site. This material presents extremely high dielectric permittivity (10^4–10^5) at a wide range of frequencies (10^2–10^6 Hz) and temperatures (100–600 K). The CCTO structure is obtained by Ti^{4+} and open-shell Cu^{2+} incorporation into perovskite without doping. Jahn–Teller distortion in Cu^{2+} is caused by a distortion of the TiO_6 octahedrons in the structure that creates a square planar structure. Moreover, the strongly covalent interaction between oxygen atoms and A′-Cu and B-Ti ions enhances the charge transfer between them, which is very important for electrocatalytic applications.[38–42]

In addition to altering the electrode material to improve POP electrochemical decomposition, changes in the active radicals also have been investigated, particularly sulfate radical-based AOPs that rely on the *in situ* generation of $^{\bullet}SO_4$ radicals through peroxymonosulfate (PMS) activation. This can be obtained using different methods, such as UV irradiation, catalysis by metal ions, electrochemistry, metal oxides, and carbon material.[23,43–45] Transition metals and their oxides are commonly used as activating species in sulfate radical-based AOPs. For instance, copper as an A′-site metal in CCTO perovskite is an effective catalyst for PMS activation for drug elimination. Indeed, Cu^{+}–Cu^{2+} and Cu^{2+}–Cu^{3+} redox pairs promote $^{\bullet}SO_4^{-}$ generation *via* PMS activation.[46–48] Hence, compared with other transition metal oxides, copper oxide (CuO) is one of the most effective catalysts for decomposing PMS into $^{\bullet}SO_4^{-}$, with low cost and limited toxicity.[49] Li *et al.* used CuO (obtained using an easy, single-step hydrothermal approach) to activate PMS for removing acid orange AO7 dye. CuO displayed excellent catalytic activity (95.38% of dye removed after 15 min) with 5 mM PMS. This indicates that CuO and PMS are good candidates for the degradation of very stable, toxic POPs (*e.g.* acid orange AO7) through the formation of ·OH and $^{\bullet}SO_4^{-}$ radicals.[50]

Researchers have also combined metal ions (Mn^{+}) to activate PMS with electrocatalysis to create an electrocatalysis/Mn^{+}/PMS system that enhances the drug removal efficiency in a short time, thus decreasing the consumption of electrical energy.[51]

In our work, we have made significant advancements in the formation of pores within CCTO, aiming to enhance the active sites available for catalysis. Additionally, we have increased the amount of the CuO phase, a step designed to effectively enhance the activation of sulfate radicals. The electrodes were prepared by pressing the CCTO powder with different amounts of polymethyl methacrylate (PMMA) using a hydraulic press. PMMA promoted pore formation and oxidation of the ex-soluted Cu_2O phase into CuO. After studying the morphology, structure, and optical characteristics of the obtained samples, paracetamol degradation in the presence of PMS was monitored to determine their electrocatalysis efficiency. Lastly, the radicals implicated in paracetamol degradation, the total organic carbon (TOC), and toxicity were determined.

2. Experimental section

2.1. Chemicals

Titanium(IV) oxide (TiO_2, 99.5%, CAS number: 13463-67-7), calcium carbonate ($CaCO_3$, 98%, CAS number: 471-34-1), PMMA (CAS number: 9011-14-7), potassium hydroxide (KOH, ≥85%, CAS number: 01900-20-08), poly(vinyl alcohol) (PVA, 99%, CAS number: 9002-89-5), paracetamol (PCM, ≥99% CAS number: 103-90-2), potassium chloride (KCl, ≥99.0%, CAS number: 7447-40-7), sodium chloride (NaCl, ≥99%, CAS number: 7647-14-5), sodium sulfate (Na_2SO_4, ≥99%, CAS number: 7757-82-6), PMS (CAS number: 70693-62-8), methanol (CH_3OH, ≥99.9%, CAS number: 67-56-1) *tert*-butanol ($(CH_3)_3COH$, ≥99.5%, CAS number: 75-65-0), and *p*-benzoquinone ($C_6H_4O_2$, ≥99.5%, CAS number: 106-51-4) were purchased from Sigma Aldrich. Copper(II) oxide (CuO, CAS number: 1317-38-0, 98%) was from Alfa Aesar. All chemicals were used without any further purification.

2.2. Preparation of CCTO porous membranes

After mixing CaO, CuO, and TiO_2 (1 : 3 : 4 mol%), as powders, in a planetary ball mill (PM200, Retsch) for 5 h (rotation speed = 350 rpm, alumina balls (powder-to-ball mass ratio of 1 : 9) in an alumina jar) and the powder was calcined at 900 °C for 3 h. Then, the powder was mixed (rotation speed = 250 rpm) with different amounts of the pore-forming agent PMMA (20, 30 and 40 wt%) for 1 h to obtain a homogeneous mixture. After milling, 5 wt% PVA was added, and the powder was pressed into pellet disks at about 9 T using a hydraulic press. Pellets (20 mm in diameter and 1–2 mm thick) were sintered in air for 3 h (2 °C min^{-1} up to 240 °C, followed by 1 °C min^{-1} up to 420 °C and 2 °C min^{-1} up to 850 °C to ensure complete PMMA burning, and then 5 °C min^{-1} up to 1100 °C). Four pellets were prepared: CCTO without PMMA (CCTO), and CCTO-20, CCTO-30 and CCTO-40 with 20, 30, and 40 wt% PMMA, respectively.

2.3. Characterization of the synthesized nanocomposites

The pellet's surface morphology, crystallinity, and composition were analyzed using scanning electron microscopy (SEM), three-dimensional (3D) optical microscopy, energy-dispersive X-ray (EDX) spectroscopy, X-ray diffraction (XRD) analysis with Rietveld refinement, Raman spectroscopy, X-ray photoelectron spectroscopy (XPS), mercury porosimetry, and electron paramagnetic resonance (EPR). The optical properties were studied using photoluminescence. Further details about the parameters and instruments can be found in the ESI† Part S1.

2.4. Electrochemical properties

For these measurements, a Solartron SI 1287 potentiostat/galvanostat, a three-electrode system, and 1 M KOH (electrolyte) were used. The samples (diameter = 2 cm), Ag/AgCl, and platinum wire were the working electrode, reference electrode, and counter electrode, respectively. Before all experiments, electrolytes were degassed with pure argon for 30 minutes to eliminate the oxygen in the solution. The sample oxidation and reduction potentials were determined by cyclic voltammetry. The interfacial charge transfer resistance of the electrode was measured by electrochemical impedance spectrometry (EIS): frequency from 0.01 Hz to 105 MHz and voltage bias of 10 mV amplitude.

2.5. Electrocatalytic system for PCM degradation

PCM was chosen as a target pollutant to assess the catalytic removal effectiveness of the prepared electrodes. PCM (initial concentration of 10 ppm), 0.5 mM PMS (active component), and 50 mM Na_2SO_4 (electrolyte solution) were added into a beaker to reach a total volume of 210 ml. The three-electrode system described in section 2.4 was used for all experiments. Before electrolysis, the solution was degassed by 30 minutes of argon bubbling to eliminate dissolved oxygen. During the entire experiment (240 minutes), the solution was stirred, and at different time-points, 1 mL aliquots were collected using a disposable syringe and filtered.

2.6. Analytical procedures

PCM concentration in the different aliquots was determined by high-performance liquid chromatography (HPLC) coupled with mass spectrometry (MS) as previously described in ref. 22 and 52. PCM elimination efficiency was then determined using the HPLC-MS data and eqn (1):[53]

$$\text{Removal efficiency (\%)} = \frac{(C_0 - C)}{C_0} \cdot 100 \quad (1)$$

where C_0 (mg L^{-1}) is the PCM concentration at time = 0, and C (mg L^{-1}) is the PCM concentration in the solution at the different time-points during electrocatalysis.

2.7. Scavenger studies

The reactive species involved in the electrocatalysis system during PCM mineralization were identified with trapping experiments by adding the following scavengers into the electrocatalysis solution: 6.6 mM *p*-benzoquinone, 660 mM *tert*-butyl alcohol, and 660 mM methanol to trap superoxide ($^{\bullet}O_2^-$), hydroxyl $^{\bullet}OH$, and sulfate ($^{\bullet}SO_4^-$) and $^{\bullet}OH$ radicals, respectively.

2.8. Toxicity tests

The acute toxicity of PCM and its intermediate by-products was assessed with a bioluminescence inhibition assay in which the bioluminescence changes[54] of the *Vibrio fischeri* LCK 487 strain are measured and analyzed using the Microtox® Model 500 analyzer (Modern Water Inc.; UK) and the MicrotoxOmni® software. The activation of *V. fischeri* is described in the ESI† Part S2. Eqn (2)[55] was used to calculate *V. fischeri* luminescence inhibition rate:

$$I(t)(\%) = \left(1 - \frac{\mathrm{LU}(t)}{R(t) \times \mathrm{LU}(0)}\right) \cdot 100 \quad (2)$$

where LU(t) is *V. fischeri* luminescence intensity after 5 min of contact with the sample, LU(0) is the initial luminescence (without sample), and $R(t)$ is the correction term. As *V. fischeri* luminescence decreases naturally over time even in a control solution (MilliQ water and NaCl), $R(t)$ is calculated with eqn (3):[2]

$$R(t) = \frac{\mathrm{LU0}(t)}{\mathrm{LU0}(0)} \cdot 100 \quad (3)$$

where LU0(t) is *V. fischeri* luminesce intensity after 5 min in the control solution and LU0(0) is the initial luminescence intensity before addition of the control solution.

2.9. TOC and energy consumption

PCM degradation was assessed by measuring the TOC of the initial and treated samples using a TOC-L CSH/CSN Shimadzu (Japan) analyzer. A TOC standard solution of 1000 mg L^{-1} was used to generate the calibration curves. TOC removal rate was calculated with eqn (4):[56]

$$\text{TOC removal } (\%) = \frac{\Delta(\mathrm{TOC})_{\mathrm{exp}}}{\mathrm{TOC}_0} \times 100 \quad (4)$$

where $\Delta(\mathrm{TOC})_{\mathrm{exp}}$ is the TOC decrease (mg L^{-1}) at the different time-points, and TOC_0 is the baseline TOC value.

The energy consumption per TOC mass unit ($\mathrm{EC_{TOC}}$) was determined with eqn (5):

$$\mathrm{EC_{TOC}}\ (\mathrm{kWh\ g_{TOC}^{-1}}) = \frac{UIt}{\Delta(\mathrm{TOC})_{\mathrm{exp}} V_s} \quad (5)$$

where U is the applied voltage (in V), I the current (in A), t the electrolysis time (in h), $\Delta(\mathrm{TOC})_{\mathrm{exp}}$ the experimental TOC decrease (g L^{-1}), and V_s the solution volume (in L).

3. Results and discussion

3.1. Characterization of the synthesized composites

The CCTO powder was mixed or not with different PMMA amounts, and after milling the pressed pellet disks were sintered (as described in Fig. S1†) to fully eliminate PMMA and to obtain porous pellets.

SEM analysis (Fig. 1) clearly indicated that all pellets had a similar morphology with the presence of two main structures: grains and grain boundary regions (between the largest grains). The CCTO-20, CCTO-30 and CCTO-40 samples presented additional voids that confirmed the formation of porous ceramics upon PMMA addition. Mercury porosimetry confirmed that CCTO porosity increased upon PMMA addition from 5.4% (0% PMMA) to ~50% in all samples, regardless of the PMMA amount used (20%–30%–40%) (Table 1). Additionally, the pore size distribution, as illustrated in Fig. 1b, demonstrates a concurrent increase in pore size with the introduction of PMMA. Specifically, the CCTO-20 sample exhibited a pore size of 39.9 μm. However, with the incorporation of 40% PMMA, the pore size in the membrane expanded to 55.1 μm (Table 1). This increase can be attributed to the agglomeration of PMMA within the membrane structure.

These results were confirmed by 3D optical microscopy that showed a homogeneous pore distribution at the surface of the CCTO-20, CCTO-30 and CCTO-40 samples (Fig. S2†).

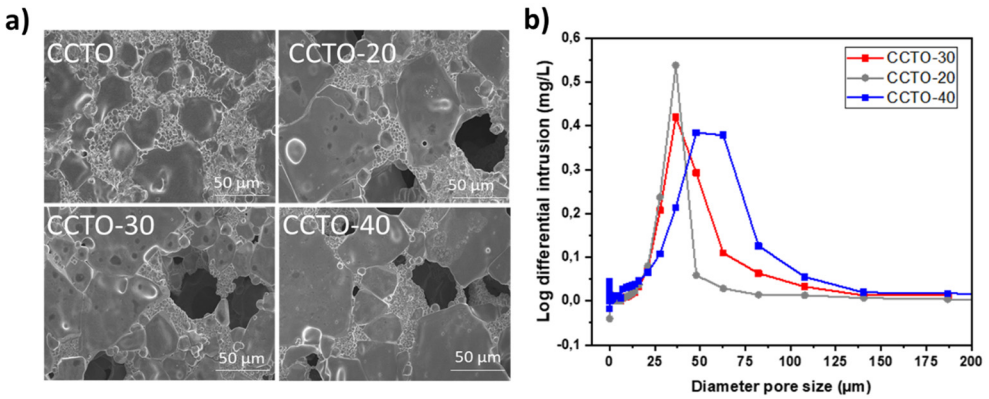

Fig. 1 (a) SEM images of the CCTO samples prepared using different amounts of PMMA (0, 20, 30, and 40 wt%) and (b) pore size distribution.

Table 1 Porosity and pore size of the CCTO samples prepared using different PMMA amounts (0, 20, 30, and 40 wt%)

Sample	Porosity (%)	Pore size (μm)
CCTO	5.4 ± 2.9	—
CCTO-20	48.0 ± 2.5	39.9 ± 2.8
CCTO-30	49.9 ± 1.6	44.7 ± 3.6
CCTO-40	51.7 ± 3.7	55.1 ± 2.1

The chemical composition and element distribution (Fig. 2), determined by EDX, revealed that Ca and Ti were present in grains, Cu in the grain boundaries, and O in both. This suggests that the CuO phase was in the boundary regions and the CCTO phase in the grains.

The main XRD patterns of the different samples after sintering could be attributed to the cubic perovskite structure of CCTO (the main crystalline phase), and the other low-intensity XRD reflections were assigned to a secondary CuO phase (Fig. 3a). PMMA addition increased the CuO phase intensity. However, in the XRD patterns of powdered samples, obtained by grinding the sintered pellets, another minor phase of Cu_2O appeared in CCTO and CCTO-40, suggesting that this phase was present mainly in the bulk of the materials (Fig. 3b). No XRD reflection corresponding to the carbon or carbide-based crystalline phase was observed, confirming PMMA thermal decomposition into volatile gaseous species upon sintering. Then, Rietveld analysis of the XRD data of the powdered samples (Cu_2O was observed only in the powdered samples) showed that in all plots (Fig. S3†), the main phase was CCTO with a minor CuO phase. The weight fraction of the CuO phase progressively increased and that of the CCTO phase decreased in samples with increasing PMMA amount (Fig. 3c). CuO phase formation, related to the eutectic point of CuO–TiO_2 (liquid phase), occurred at the sample surface. At this point, atoms can migrate and diffuse easily between grains and grain boundaries. Moreover, it has been reported that Cu^{2+} is not stable at high temperature and tends to be reduced to Cu^{+}. Consequently, Ti^{4+} may be substituted at Cu sites for charge compensation or a Cu_2O phase may be formed.[57] Upon cooling, Cu^{+} might donate electrons to the Ti 3d conduction band and convert back to Cu^{2+}, forming a CuO phase.[57] The CuO phase in grain boundaries might be explained by CuO migration into such regions during the cooling, as reported in our previous studies.[38,40] The CCTO sample also contained 3.2 wt% Cu_2O, presumably due to the limited oxygen diffusion from the surface to the bulk in the absence of a porous morphology. However, when PMMA was added to CCTO, CuO was mainly detected and only negligible amounts of Cu_2O, suggesting the Cu_2O side phase oxidation into CuO due to enhanced oxygen diffusion in the pores formed upon PMMA addition. In CCTO-40, 1.0 wt% of Cu_2O still remained in the sample, possibly due to PMMA agglomeration when at higher concentrations. In this sample, PMMA agglomeration

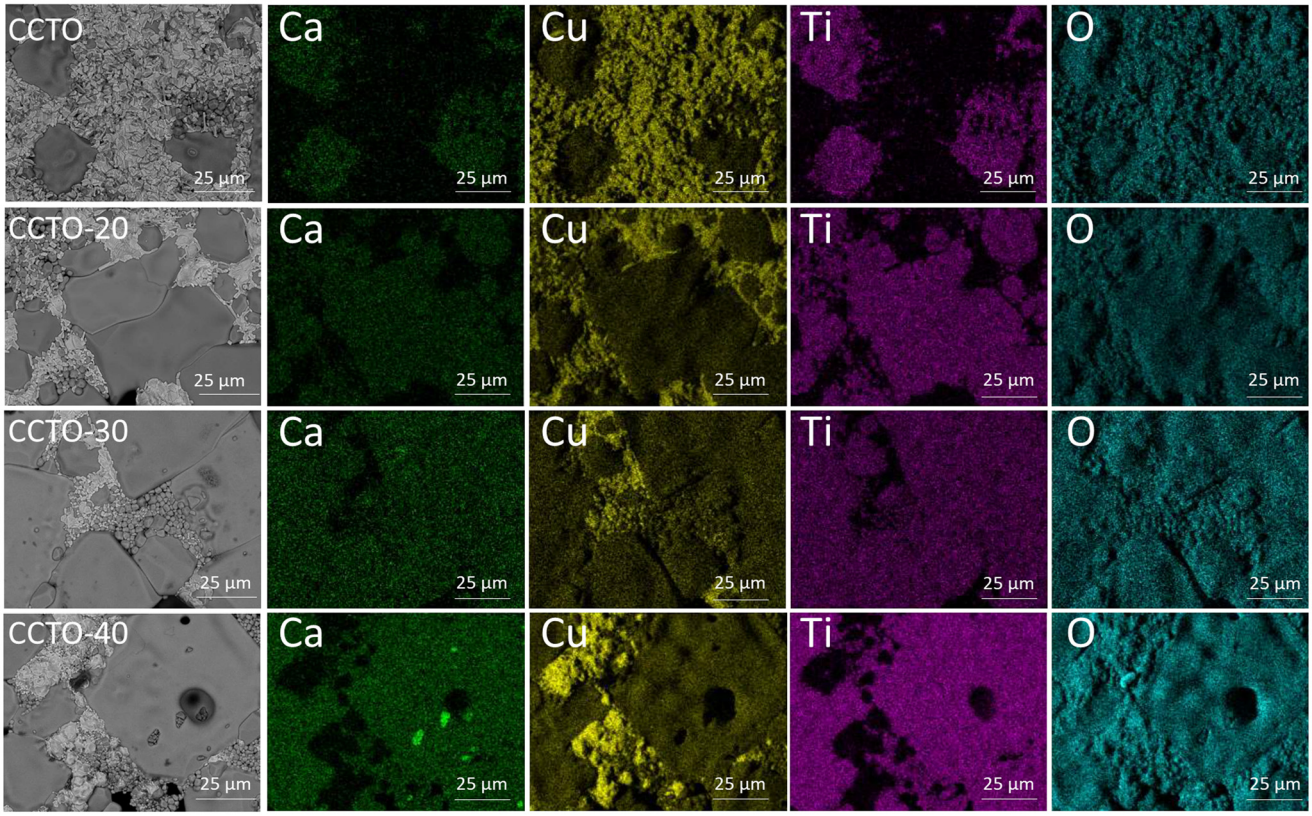

Fig. 2 SEM/EDX mapping of the CCTO samples prepared using different PMMA amounts (0, 20, 30, and 40 wt%).

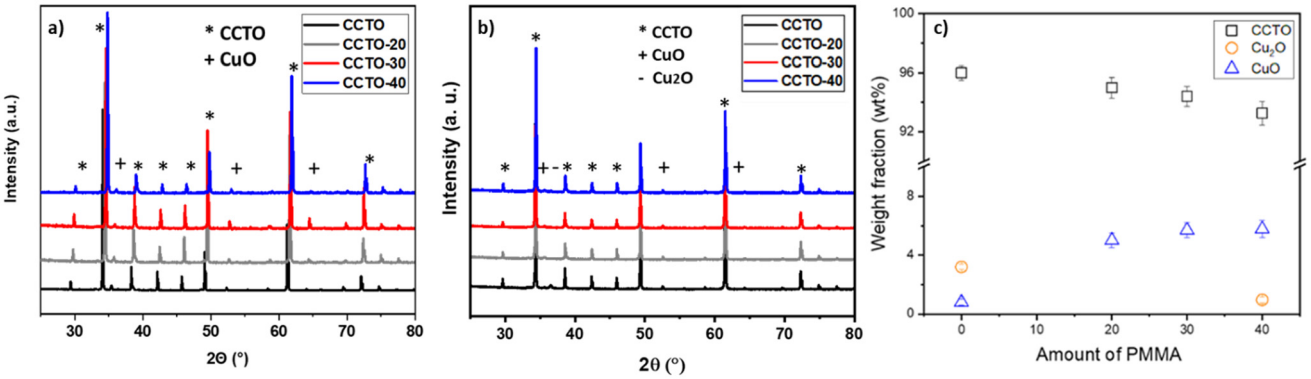

Fig. 3 (a) XRD patterns of CCTO pellets prepared using different amounts of PMMA (0, 20, 30, and 40 wt%). (b) XRD patterns of the same samples after powdering. (c) Weight fraction of the formed crystalline phases (Rietveld analysis of the XRD data for the powdered samples).

might limit Cu_2O oxidation. Furthermore, higher PMMA concentrations led to increased carbon in the sample that can react with oxygen and limit the diffusion into the bulk.

Raman spectroscopy (Fig. 4a) clearly showed two strong bands at 445 cm^{-1} and 510 cm^{-1}, and a weaker band at 291 cm^{-1}. The 445 cm^{-1} band was assigned to $A_g(1)$, and the 512 cm^{-1} band to $A_g(2)$. These are pseudo-modes that originated in the $[TiO_6]$ cluster oscillation within the CCTO structure. The 291 cm^{-1} band was assigned to the CuO mode.[58] Raman mapping was used to confirm the elements present in the grains and grain boundaries. The grains (orange) and grain boundary regions (black) were perfectly separated in the Raman image at 510 cm^{-1} (Fig. 4b), and the peak intensity corresponded to the $A_g(2)$ mode of CCTO. The peak at 291 cm^{-1} (Fig. 4c) was assigned to the Raman active mode of CuO, which is shown in black in the grains and in orange in the grain boundaries.[59] These results confirmed the SEM/EDX results, which suggested that CuO is present at the grain boundaries and CCTO in the grains. The Raman peak shift was explained by the CuO phase formation in grain boundaries and the CCTO phase deformation.[60] To obtain more details on the chemical compositions and chemical states, the different samples were characterized by XPS. Cu, Ti and O with different chemical states were detected in all samples. Fig. 4d shows the high-resolution Cu 2p spectra and the Cu $2p_{3/2}$ (934.5 eV) and Cu $2p_{1/2}$ (954.2 eV) peaks.[59,61,62] After deconvolution, in the CCTO spectrum, the Cu $2p_{3/2}$ and Cu $2p_{1/2}$ peaks were each composed of two peaks. The two main peaks (954 eV and 932 eV) were assigned to Cu^{2+}, and the two small shoulder peaks (951.5 eV and 931.5 eV) to Cu^{1+}, as expected for Cu_2O. Shake-up satellites (937 to 945 eV), typical of Cu^{2+}, also were present. In CCTO-20 and CCTO-30, prepared with 20 and 30 wt% PMMA, respectively, the peaks related to Cu^{1+} were not detected. This confirmed the Rietveld refinement results, suggesting that the Cu_2O phase was oxidized to CuO at high temperatures due to the formation of pores that facilitate oxygen diffusion.[62,63] In CCTO-40 (40% PMMA), the shoulder peaks of Cu^{1+} reappeared, in agreement with the XRD measurements showing the Cu_2O phase in this sample. Fig. 4e shows the high-resolution Ti 2p spectra and the Ti $2p_{3/2}$ (458.8 eV) and Ti $2p_{1/2}$ (463.3 eV) peaks. After deconvolution, this spectrum included four peaks: two peaks at 457.8 eV and 463.9 eV (assigned to Ti^{4+}) and two peaks at 458.5 eV and 464.3 eV (Ti^{3+}). The binding energies at 459.1 eV were assigned to TiO_5 clusters.[64,65] The Ti 2p peaks were slightly shifted to higher binding energy (+0.2 eV and +0.3 eV) upon PMMA addition due to the formation of the CuO phase and of oxygen vacancies in the TiO_2 lattice that promote electron attraction.[21] The O 1s spectra after deconvolution (Fig. 4f) included peaks at 529.43 eV (assigned to the Cu–O bond), at 530 eV (Ti–O bond), and at 532.08 eV (surface adsorbed oxygen, *i.e.* adsorbed water).[38,40]

The electronic and structural characteristics of the samples were correlated using photoluminescence measurements. Fig. 5a shows the photoluminescence curves of the CCTO, CCTO-20, CCTO-30, and CCTO-40 samples at room temperature. All samples had a peak with a maximum intensity at ~370 nm, attributed to valence band transitions within TiO_6 clusters.[66,67] In the emission spectra, the shoulder at 375 nm was explained by shallow defects near the conductance band.[67] It has been reported that TiO_6 clusters are responsible for photoluminescence in CCTO, whereas formation of TiO_5 clusters leads to photoluminescence quenching.[68] The change in the balance between TiO_6 and TiO_5 might explain the observed photoluminescence quenching.[68] All samples displayed similar spectral shapes, suggesting that all materials had a very similar electronic band structure.[40] In the samples with PMMA, the overall photoluminescence intensity decrease, without shifts in peak positions, suggests an increase in the concentration of specific surface defects in the CCTO material that might promote separation of the photogenerated charges.[66,69,70] The intensity decrease was most pronounced in the CCTO-30 sample.

The EPR spectra (Fig. 5b) of all samples showed a strong signal of comparable (double-integrated) intensity at g = ~2.15, which was previously attributed to Cu^{2+} species.[71] This finding suggests that the amount of Cu^{2+} species was similar in all studied samples. Yet, in the CCTO-30 sample, the

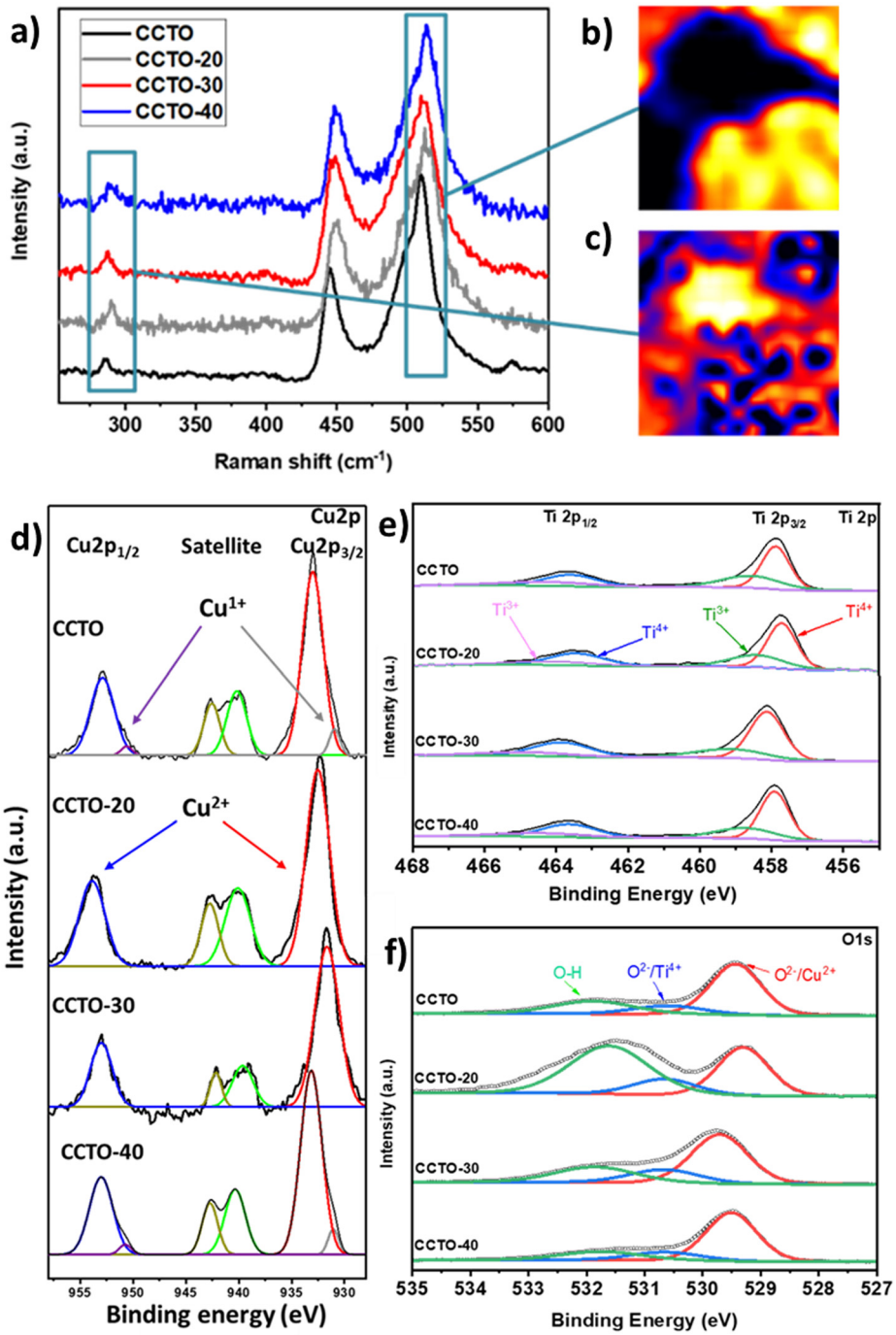

Fig. 4 (a) Raman shifts of the CCTO samples prepared using different PMMA amounts (0, 20, 30, and 40 wt%). (b and c) Raman maps: (b) 510 cm^{-1} (CCTO) and (c) 291 cm^{-1} (CuO). (d–f) High-resolution XPS spectra of (d) Cu $2p_{3/2}$, (e) Ti $2p_{3/2}$, and 9f) O 1s for the CCTO samples prepared using different PMMA amounts (0, 20, 30, and 40 wt%).

amplitude was clearly smaller (by a factor of ~2) and the ΔB_{pp} linewidth larger compared with the other samples (~5 mT *versus* ~3.3 mT). This is indicative of altered spin-interactions of the detected Cu^{2+} species. Like for the decreased photoluminescence intensity of the CCTO-30 sample, this change may be linked to a modification of defects in CCTO.

The electrochemical properties of the CCTO pellets with/without different amounts of PMMA were investigated using a three-electrode system in 1 M KOH. In the cyclic voltammetry curves (scan rate of 25 mV s^{-1} in the potential range of 0–1 V *vs.* Ag/AgCl) (Fig. 6a), CuO oxidation and reduction peaks were detected. CCTO displayed the lowest intensity compared with the porous CCTO samples prepared using PMMA. This can be attributed to the better contact and wettability of the porous CCTO-20, CCTO-30 and CCTO-40 samples in the electrolyte solution.[62,72] Moreover, CCTO-30 had the highest current density (0.82 mA cm^{-2} *versus* 0.63 and 0.71 mA cm^{-2} for CCTO-

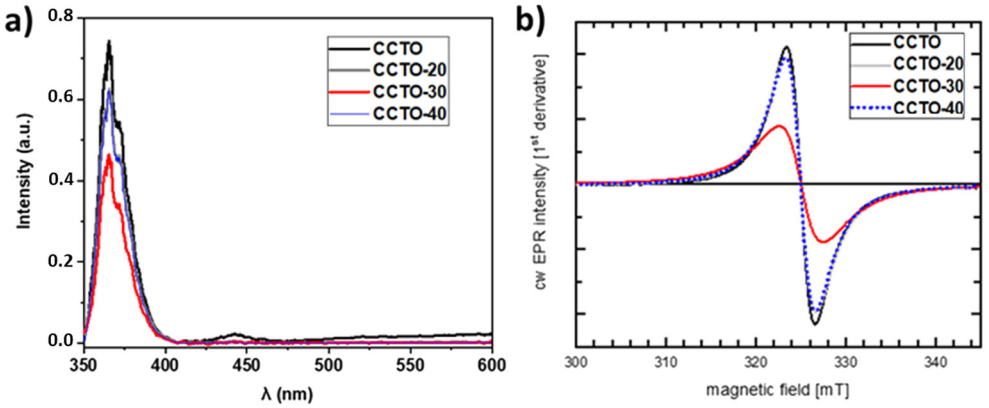

Fig. 5 (a) Photoluminescence spectra and (b) room-temperature cw EPR spectra of the CCTO-20, CCTO-30, CCTO-40 and CCTO samples.

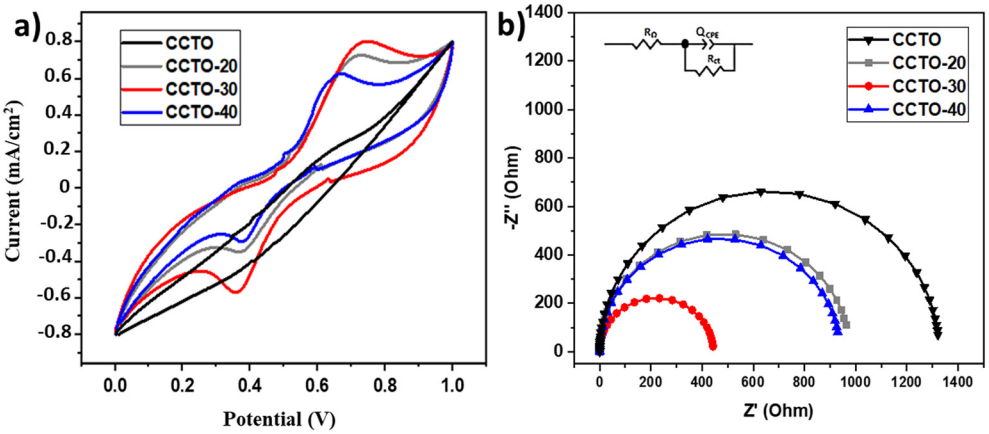

Fig. 6 (a) Cyclic voltammetry curves obtained using CCTO, CCTO-20, CCTO-30 and CCTO-40 as electrodes in 1 M KOH (scan rate = 25 mV s^{-1}). (b) Nyquist plots showing the electrochemical impedance spectroscopy data for CCTO, CCTO-20, CCTO-30 and CCTO-40.

40 and CCTO-20, respectively). This result may be related to the higher weight fraction of the CuO phase in the CCTO-30 sample (verified by the Rietveld refinement analysis of XRD data) and the formation of defects (indicated by the photoluminescence and EPR results), such as oxygen vacancies, that expose more active surface sites.[73,74] The cyclic voltammetry data were in agreement with the EIS results (Fig. 6b). Data were fitted with the Z-View software and the equivalent electrical circuit $R + Q_{CPE}//R_{ct}$ (R = electrolyte resistance, Q_{CPE} = constant phase element, and R_{ct} = charge transfer resistance). The EIS plot shows that CCTO displayed the highest arc radius compared with the CCTO samples with PMMA. This indicates an increase in the charge transfer capacity following the formation of pores and the increase in surface contact. Comparison of the resistance values of CCTO, CCTO-20, CCTO-30, and CCTO-40 indicated that CCTO-30 had the fastest interfacial charge migration. This may be related to the increase in the CuO phase and in the defect amount, presumably oxygen vacancies, that facilitate charge transfer in CCTO-30.[75,76]

The electrocatalytic activity of CCTO samples with/without PMMA as anodes was evaluated by following the degradation of 10 ppm PCM in 210 mL of sodium sulfate (electrolyte solution) with 0.5 mM of PMS (active component) at the fixed potential of 1.5 V *vs.* Ag/AgCl (Fig. S4†). PCM degradation was limited to 64% with CCTO, even after 4 h. Conversely, with the porous CCTO samples prepared using different PMMA amounts, PCM was completely removed after 90 min (CCTO-30), 150 min (CCTO-40), and 210 min (CCTO-20) (Fig. 7a and b). Thus, PMMA addition clearly improved PCM removal efficiency. CCTO-30 was the most effective and faster anode for PCM degradation. This could be explained by the high charge transfer (EIS data) linked to the increase in defects, and the CuO phase amount. The generation of oxygen vacancies may allow producing more active defects, thus enhancing the electrochemical degradation of pollutants.[77,78] Furthermore, based on literature data, the CuO phase promotes PMS activation to produce $SO_4^{\cdot-}$ free radicals, according to eqn (6).[48] In addition, the Cu(II)–HSO_5 combination might yield both Cu(III) and ·OH by an alternative mechanism of one-electron transfer (eqn (7)). It has been shown that these radical Cu(III) species act as a selective oxidant (eqn (8)) for PCM removal due to their reducing potential (1.57–2.3 V).[79,80]

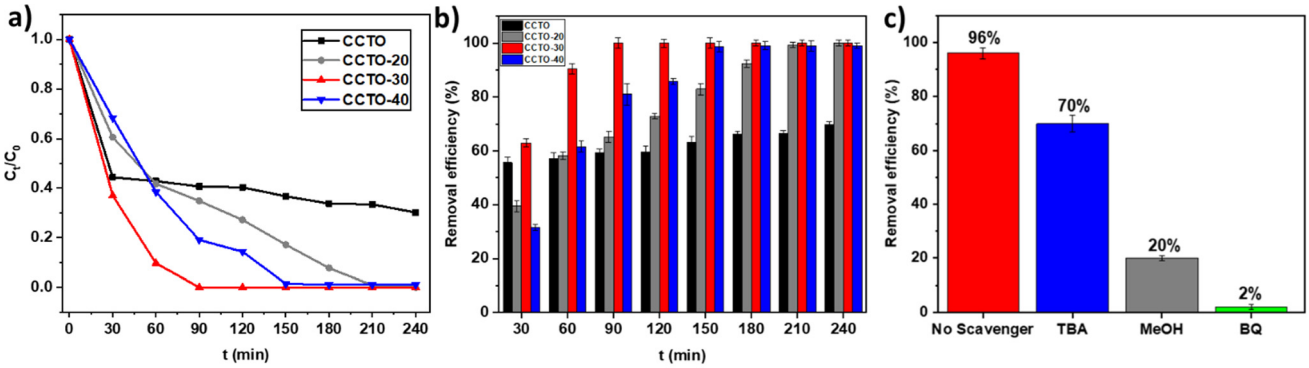

Fig. 7 (a) PCM degradation by electrocatalysis *via* PMS activation. (b) PCM removal efficiency. (c) Radical scavengers test. TBA: *tert*-butanol (·OH scavenger); MeOH: methanol (·OH and $^{\bullet}SO$ scavenger); BQ: *p*-benzoquinone ($^{\bullet}O_2^-$ scavenger).

$$Cu^{2+} + HSO_5^- \rightarrow Cu^{1+} + SO_4^{\bullet-} + OH^- \quad (6)$$

$$Cu^{2+} + HSO_5^- \rightarrow Cu^{3+} + SO_4^{2-} + OH^{\bullet} \quad (7)$$

$$Cu^{3+} + \text{organic pollutants} \rightarrow Cu^{2+} + \text{oxidation products} \quad (8)$$

$$SO_4^-/^{\bullet}OH + \text{organic pollutants} \rightarrow SO_4^{2-}/H_2O + \text{oxidation products} \quad (9)$$

$$e^- + O_2 \rightarrow {}^{\bullet}O_2^- \quad (10)$$

To better assess the role of oxidizing radicals in PCM degradation, the degradation of 10 ppm PCM in 210 mL of sodium sulfate electrolyte solution with 0.5 mM PMS was monitored in the presence of radical scavengers. PCM degradation strongly decreased, from 96% to 70%, in the presence of *tert*-butanol, a well-known ·OH scavenger[22,81] (Fig. 7c). PCM degradation was reduced to 20% when methanol (a scavenger for ·OH and $^{\bullet}SO^{4-}$)[82] was used, and to 2% with *p*-benzoquinone (a scavenger of $^{\bullet}O_2^-$).[52] This suggests that $^{\bullet}O_2^-$ radicals play a key role in PCM degradation in the presence of PMS. Overall, this study revealed that $^{\bullet}SO_4^-$ and $^{\bullet}O_2^-$ radicals were the main reactive species, whereas ·OH radicals were only a minor species in PCM degradation.

The stability of the CCTO-30 anode was monitored during five successive cycles (anode rinsed in deionized water several times after each cycle). CCTO-30 pellets remained stable without losing activity after five cycles, demonstrating their potential as a reusable electrocatalyst (Fig. 8a).

To evaluate the effect of PMS on the electrocatalytic process, different systems were tested for PCM degradation. No PCM degradation was observed in the systems with only CCTO and with only PMS (Fig. 8b) at room temperature.[83] In the electrocatalysis (EC)–CCTO-30 binary system, only 6.8% of PCM was degraded, possibly because not enough radicals are produced to completely degrade organic molecules. Even in the PMS–CCTO-30 system, only 8.5% of PCM was removed, confirming the need of anodic oxidation.[84] Conversely, when electrocatalysis and PMS–CCTO-30 were coupled (EC–PMS–CCTO-30), PMS was efficiently activated and 100% of PCM was degraded in 90 min. This improvement was also the result of PMS activation forced by the electron transfer occurring at the anode surface.[85] The much higher PCM degradation obtained with the EC–PMS–CCTO-30 system (100.0%), compared with the EC–CCTO-30 (6.8%) and PMS–CCTO-30 (8.5%) systems, indicates the existence of a distinct, synergistic effect between electrocatalysis and PMS–CCTO-30.[86]

TOC content was quantified to determine the degree of PCM degradation using CCTO-30 as anode. TOC rapidly decreased in the first 60 minutes (Fig. 8c).[87,88] The TOC removal rate of 42.7 ± 2.1% at 4 h suggested PCM degradation into other smaller organic compounds. At longer time points, mineralization gradually increased due to the development of degradation by-products (*e.g.* short-chain carboxylic acids and aliphatic organic acids, such as fumaric, oxalic, acetic, and maleic acids) with slower radical reaction kinetics.[2,89] Indeed, TOC was still not completely eliminated after 12 h of reaction.[56,90]

As the aim of wastewater treatments is to reduce harmful substances, it was important to study the toxicity of PCM and also of these smaller chain aliphatic organic acids that persisted in solution. First, *V. fischeri* bioluminescence inhibition was 74% upon PCM addiction (Fig. 8d). After 1 h of PCM degradation, inhibition increased to 79%, suggesting the formation of even more hazardous by-products, for instance *p*-benzoquinone, benzaldehyde and benzoic acid.[2,85,90] After 2 h of electrocatalysis, bioluminescence intensity inhibition decreased to ~9%, indicating the decomposition of these hazardous intermediate by-products to less harmful chemicals.[91] After 10 h, luminescence inhibition was very low, suggesting a complete transformation of PCM and its by-products into non-toxic compounds.[21]

The energy consumption per TOC was 1.45 kW h g_{TOC}^{-1}. This is a relatively low energy consumption compared with previous studies on PCM mineralization (*e.g.* 3.6 kW h g_{TOC}^{-1} for PCM mineralization using electro-Fenton).[2]

In recent years, perovskite materials have attracted much attention as highly active anodes for wastewater treatment by electrocatalytic oxidation. As the CCTO perovskite used in this work has not been studied before as an anode in electrocatalytic

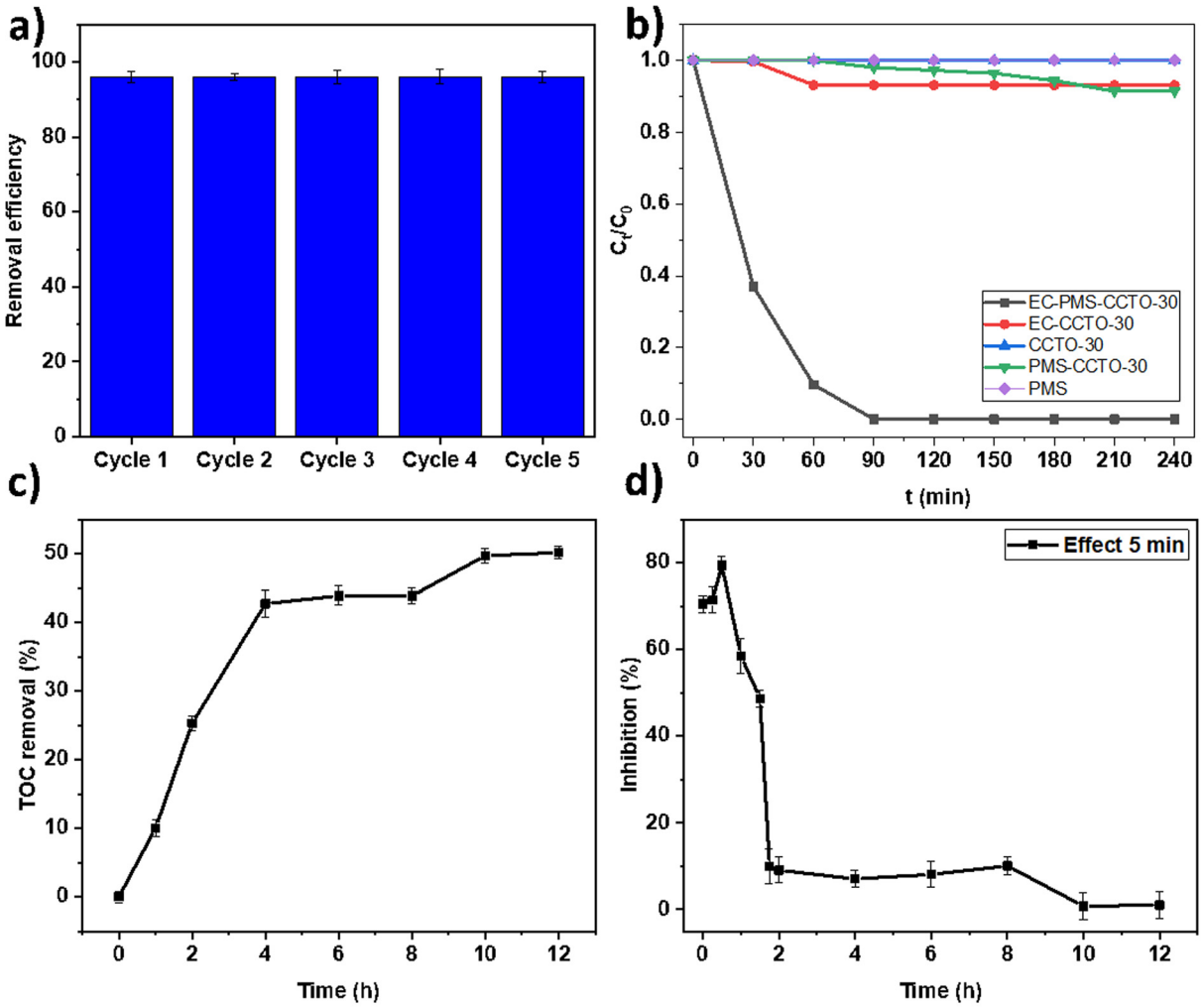

Fig. 8 (a) Reusability of CCTO-30 over five successive cycles. (b) PCM removal using different systems. (c) TOC removal during PCM degradation (EC–PMS–CCTO-30 system). (d) *Vibrio fischeri* luminescence inhibition during PCM degradation.

Table 2 Comparison of studies on the use of perovskite anodes for the electrocatalytic degradation of organic pollutants

Pollutant	$C_{pollutant}$ (mg L^{-1})	Anode material	Current or voltage	Solution volume (mL)	pH	Degradation time	Removal efficiency (%)	Ref.
Methyl red	140	$Ti/CoTiO_3/Ce–PbO_2$	30 mA cm^{-2}	100	7	180	90	92
Tetracycline hydrochloride	20	$Cu_xCo_{1-x}Mn_2O_4$/Ti (14.24 cm^2)	1.70 V	250	3	120	91.3	37
Methyl orange	20	$Sr_xLa_{1-x}Mn_yCo_{1-y}O_{3-\delta}$ (16 cm^2)	20 mA cm^{-2}	200	9	60	99.61	93
Ciprofloxacin	5	$BiFeO_3$ with graphite nanoparticles	1.5 V	75	6.8	240	36	94
Paracetamol	10	CCTO-30 (3.14 cm^2)	1.5 V	210	7	90	100	This work

water remediation, its performance was compared with that of other perovskite catalysts (summary in Table 2). Although the direct comparison was hampered by differences in decomposition set-ups, the CCTO-30 electrode showed high degradation efficiency in a short time (90 min) and with low electricity consumption, despite a similar small surface area per gram (3.14 cm^2), compared with other perovskite anodes. This indicates that this CCTO material could be a promising anode for electrochemical wastewater treatment.

4. Conclusion

In summary, porous calcium copper titanate (CCTO) pellets were synthesized by adding polymethyl methacrylate (PMMA) as a pore-forming agent to CCTO powder before ball milling, pressing, and thermal treatment under air atmosphere. 3D microscopy images confirmed the homogenous pore distribution in the obtained ceramic pellets due to PMMA thermal decomposition, yielding

porosities of ~50%. Electrochemical measurements revealed that CCTO-30 (with 30% PMMA) contained the highest amount of CuO phase and displayed the lowest resistance, the highest charge transfer capacity, and the highest redox peaks. Then, all samples were tested as anodes for paracetamol (PCM) degradation *via* peroxymonosulfate (PMS) activation. Total PCM removal was achieved by the CCTO-30 electrode after 90 min. Moreover, this sample remained stable without loss of activity after five cycles. The scavenging test experiments revealed the major role of $\cdot SO_4^-$ and $\cdot O_2^-$ radicals and the minor role of ·OH radicals in PCM degradation. Thus, the fabrication of porous CCTO electrodes using PMMA is a suitable approach for the development of electrocatalysis materials in the advanced oxidation processes (AOPs) field to remove persistent organic pollutants (POPs) from wastewater.

Conflicts of interest

There are no conflicts to declare.

Acknowledgements

This project has received funding from the Research Council of Lithuania (LMTLT), the GILIBERT 2021 program agreement No S-LZ-21-4 and was co-founded by Campus France grant No. 46593RA (PHC GILIBERT 2021).

References

1 S. Puri, I. Thakur, A. Verma and S. Barman, Degradation of Pharmaceutical Drug Paracetamol via UV Irradiation Using Fe-TiO2 Composite Photocatalyst: Statistical Analysis and Parametric Optimization, *Environ. Sci. Pollut. Res.*, 2021, **28**(34), 47327–47341, DOI: **10.1007/s11356-021-13895-6**.

2 T. X. H. Le, T. V. Nguyen, Z. Amadou Yacouba, L. Zoungrana, F. Avril, D. L. Nguyen, E. Petit, J. Mendret, V. Bonniol, M. Bechelany, S. Lacour, G. Lesage and M. Cretin, Correlation between Degradation Pathway and Toxicity of Acetaminophen and Its By-Products by Using the Electro-Fenton Process in Aqueous Media, *Chemosphere*, 2017, **172**, 1–9, DOI: **10.1016/j.chemosphere.2016.12.060**.

3 H. B. Quesada, A. T. A. Baptista, L. F. Cusioli, D. Seibert, C. de Oliveira Bezerra and R. Bergamasco, Surface Water Pollution by Pharmaceuticals and an Alternative of Removal by Low-Cost Adsorbents: A Review, *Chemosphere*, 2019, **222**, 766–780, DOI: **10.1016/j.chemosphere.2019.02.009**.

4 Y. Yang, X. Li, C. Zhou, W. Xiong, G. Zeng, D. Huang, C. Zhang, W. Wang, B. Song, X. Tang, X. Li and H. Guo, Recent Advances in Application of Graphitic Carbon Nitride-Based Catalysts for Degrading Organic Contaminants in Water through Advanced Oxidation Processes beyond Photocatalysis: A Critical Review, *Water Res.*, 2020, **184**, 116200, DOI: **10.1016/j.watres.2020.116200**.

5 I. Sirés and E. Brillas, Remediation of Water Pollution Caused by Pharmaceutical Residues Based on Electrochemical Separation and Degradation Technologies: A Review, *Environ. Int.*, 2012, **40**, 212–229, DOI: **10.1016/j.envint.2011.07.012**.

6 W. Ren, J. Gao, C. Lei, Y. Xie, Y. Cai, Q. Ni and J. Yao, Recyclable Metal-Organic Framework/Cellulose Aerogels for Activating Peroxymonosulfate to Degrade Organic Pollutants, *Chem. Eng. J.*, 2018, **349**, 766–774, DOI: **10.1016/j.cej.2018.05.143**.

7 N. Lin, Y. Gong, R. Wang, Y. Wang and X. Zhang, Critical Review of Perovskite-Based Materials in Advanced Oxidation System for Wastewater Treatment: Design, Applications and Mechanisms, *J. Hazard. Mater.*, 2022, **424**, 127637, DOI: **10.1016/j.jhazmat.2021.127637**.

8 D. Zhu and Q. Zhou, Action and Mechanism of Semiconductor Photocatalysis on Degradation of Organic Pollutants in Water Treatment: A Review, *Environ. Nanotechnol., Monit. Manage.*, 2019, **12**, 100255, DOI: **10.1016/j.enmm.2019.100255**.

9 M. Abid, E. Makhoul, F. Tanos, I. Iatsunskyi, E. Coy, G. Lesage, M. Cretin, D. Cornu, A. Ben Haj Amara and M. Bechelany, N-Doped HNT/TiO2 Nanocomposite by Electrospinning for Acetaminophen Degradation, *Membranes*, 2023, **13**(2), 204, DOI: **10.3390/membranes13020204**.

10 D. Papagiannaki, M. H. Belay, N. P. F. Gonçalves, E. Robotti, A. Bianco-Prevot, R. Binetti and P. Calza, From Monitoring to Treatment, How to Improve Water Quality: The Pharmaceuticals Case, *Chem. Eng. J. Adv.*, 2022, **10**, 100245, DOI: **10.1016/j.ceja.2022.100245**.

11 L. Bijlsma, E. Pitarch, E. Fonseca, M. Ibáñez, A. M. Botero, J. Claros, L. Pastor and F. Hernández, Investigation of Pharmaceuticals in a Conventional Wastewater Treatment Plant: Removal Efficiency, Seasonal Variation and Impact of a Nearby Hospital, *J. Environ. Chem. Eng.*, 2021, **9**(4), 105548, DOI: **10.1016/j.jece.2021.105548**.

12 E. Bustos Bustos, A. Sandoval-González and C. Martínez-Sánchez, Detection and Treatment of Persistent Pollutants in Water: General Review of Pharmaceutical Products, *ChemElectroChem*, 2022, **9**(12), e202200188, DOI: **10.1002/celc.202200188**.

13 J. L. Wang and L. J. Xu, Advanced Oxidation Processes for Wastewater Treatment: Formation of Hydroxyl Radical and Application, *Crit. Rev. Environ. Sci. Technol.*, 2012, **42**(3), 251–325, DOI: **10.1080/10643389.2010.507698**.

14 J. Wang and R. Zhuan, Degradation of Antibiotics by Advanced Oxidation Processes: An Overview, *Sci. Total Environ.*, 2020, **701**, 135023, DOI: **10.1016/j.scitotenv.2019.135023**.

15 Y. Liu, Y. Zhao and J. Wang, Fenton/Fenton-like Processes with in-Situ Production of Hydrogen Peroxide/Hydroxyl Radical for Degradation of Emerging Contaminants: Advances and Prospects, *J. Hazard. Mater.*, 2021, **404**, 124191, DOI: **10.1016/j.jhazmat.2020.124191**.

16 Y. Liu and J. Wang, Multivalent Metal Catalysts in Fenton/Fenton-like Oxidation System: A Critical Review, *Chem. Eng. J.*, 2023, **466**, 143147, DOI: **10.1016/j.cej.2023.143147**.

17 J. Wang and S. Wang, Removal of Pharmaceuticals and Personal Care Products (PPCPs) from Wastewater: A Review,

J.Environ. Manage., 2016, **182**, 620–640, DOI: **10.1016/j.jenvman.2016.07.049**.

18 D. Kanakaraju, B. D. Glass and M. Oelgemöller, Advanced Oxidation Process-Mediated Removal of Pharmaceuticals from Water: A Review, *J. Environ. Manage.*, 2018, **219**, 189–207, DOI: **10.1016/j.jenvman.2018.04.103**.

19 F. Mansouri, K. Chouchene, N. Roche and M. Ksibi, Removal of Pharmaceuticals from Water by Adsorption and Advanced Oxidation Processes: State of the Art and Trends, *Appl. Sci.*, 2021, **11**(14), 6659, DOI: **10.3390/app11146659**.

20 Z. Masood, A. Ikhlaq, A. Akram, U. Y. Qazi, O. S. Rizvi, R. Javaid, A. Alazmi, M. Madkour and F. Qi, Application of Nanocatalysts in Advanced Oxidation Processes for Wastewater Purification: Challenges and Future Prospects, *Catalysts*, 2022, **12**(7), 741, DOI: **10.3390/catal12070741**.

21 S. Sayegh, F. Tanos, A. Nada, G. Lesage, F. Zaviska, E. Petit, V. Rouessac, I. Iatsunskyi, E. Coy, R. Viter, D. Damberga, M. Weber, A. Razzouk, J. Stephan and M. Bechelany, Tunable TiO_2 –BN–Pd Nanofibers by Combining Electrospinning and Atomic Layer Deposition to Enhance Photodegradation of Acetaminophen, *Dalton Trans.*, 2022, **51**(7), 2674–2695, DOI: **10.1039/D1DT03715C**.

22 M. Abid, S. Sayegh, I. Iatsunskyi, E. Coy, G. Lesage, A. Ramanavicius, A. Ben Haj Amara and M. Bechelany, Design of Halloysite-Based Nanocomposites by Electrospinning for Water Treatment, *Colloids Surf., A*, 2022, **651**, 129696, DOI: **10.1016/j.colsurfa.2022.129696**.

23 X. Li, B. Jie, H. Lin, Z. Deng, J. Qian, Y. Yang and X. Zhang, Application of Sulfate Radicals-Based Advanced Oxidation Technology in Degradation of Trace Organic Contaminants (TrOCs): Recent Advances and Prospects, *J. Environ. Manage.*, 2022, **308**, 114664, DOI: **10.1016/j.jenvman.2022.114664**.

24 I. Lozano, C. J. Pérez-Guzmán, A. Mora, J. Mahlknecht, C. L. Aguilar and P. Cervantes-Avilés, Pharmaceuticals and Personal Care Products in Water Streams: Occurrence, Detection, and Removal by Electrochemical Advanced Oxidation Processes, *Sci. Total Environ.*, 2022, **827**, 154348, DOI: **10.1016/j.scitotenv.2022.154348**.

25 T. Zhang, Y. Liu, L. Yang, W. Li, W. Wang and P. Liu, Ti–Sn–Ce/Bamboo Biochar Particle Electrodes for Enhanced Electrocatalytic Treatment of Coking Wastewater in a Three-Dimensional Electrochemical Reaction System, *J. Cleaner Prod.*, 2020, **258**, 120273, DOI: **10.1016/j.jclepro.2020.120273**.

26 M. El Kateb, C. Trellu, A. Darwich, M. Rivallin, M. Bechelany, S. Nagarajan, S. Lacour, N. Bellakhal, G. Lesage, M. Héran and M. Cretin, Electrochemical Advanced Oxidation Processes Using Novel Electrode Materials for Mineralization and Biodegradability Enhancement of Nanofiltration Concentrate of Landfill Leachates, *Water Res.*, 2019, **162**, 446–455, DOI: **10.1016/j.watres.2019.07.005**.

27 J. Xie, C. Zhang and T. D. Waite, Hydroxyl Radicals in Anodic Oxidation Systems: Generation, Identification and Quantification, *Water Res.*, 2022, **217**, 118425, DOI: **10.1016/j.watres.2022.118425**.

28 S. Guo, Z. Xu, W. Hu, D. Yang, X. Wang, H. Xu, X. Xu, Z. Long and W. Yan, Progress in Preparation and Application of Titanium Sub-Oxides Electrode in Electrocatalytic Degradation for Wastewater Treatment, *Catalysts*, 2022, **12**(6), 618, DOI: **10.3390/catal12060618**.

29 A. A. Ghani, N. Maile, K. Tahir, B. Kim, Y. Lim, J. Jang and D. S. Lee, Electrocatalytic Oxidation of Antidiabetic Drug Metformin Adsorbed on Intercalated MXene, *Chemosphere*, 2022, **307**, 135767, DOI: **10.1016/j.chemosphere.2022.135767**.

30 H. Jing, H. Yang, X. Yu, C. Hu, R. Li and H. Li, Treatment of Organic Matter and Ammonia Nitrogen in Wastewater by Electrocatalytic Oxidation: A Review of Anode Material Preparation, *Environ. Sci.: Water Res. Technol.*, 2022, **8**(2), 226–248, DOI: **10.1039/D1EW00695A**.

31 Y. Jiang, H. Zhao, J. Liang, L. Yue, T. Li, Y. Luo, Q. Liu, S. Lu, A. M. Asiri, Z. Gong and X. Sun, Anodic Oxidation for the Degradation of Organic Pollutants: Anode Materials, Operating Conditions and Mechanisms. A Mini Review, *Electrochem. Commun.*, 2021, **123**, 106912, DOI: **10.1016/j.elecom.2020.106912**.

32 C. A. Martínez-Huitle and S. Ferro, Electrochemical Oxidation of Organic Pollutants for the Wastewater Treatment: Direct and Indirect Processes, *Chem. Soc. Rev.*, 2006, **35**(12), 1324–1340, DOI: **10.1039/B517632H**.

33 C. Hu, Q. Zhao, G.-L. Zang, J.-T. Luo and Q. Liu, Preparation and Characterization of a Novel Ni-Doped TiO2 Nanotube-Modified Inactive Electrocatalytic Electrode for the Electrocatalytic Degradation of Phenol Wastewater, *Electrochim. Acta*, 2022, **405**, 139758, DOI: **10.1016/j.electacta.2021.139758**.

34 S. Wu and Y. H. Hu, A Comprehensive Review on Catalysts for Electrocatalytic and Photoelectrocatalytic Degradation of Antibiotics, *Chem. Eng. J.*, 2021, **409**, 127739, DOI: **10.1016/j.cej.2020.127739**.

35 W. Nabgan, M. Saeed, A. A. Jalil, B. Nabgan, Y. Gambo, M. W. Ali, M. Ikram, A. A. Fauzi, A. H. K. Owgi, I. Hussain, A. A. Thahe, X. Hu, N. S. Hassan, A. Sherryna, A. Kadier and M. Y. Mohamud, A State of the Art Review on Electrochemical Technique for the Remediation of Pharmaceuticals Containing Wastewater, *Environ. Res.*, 2022, **210**, 112975, DOI: **10.1016/j.envres.2022.112975**.

36 X. Li, H. Zhao, J. Liang, Y. Luo, G. Chen, X. Shi, S. Lu, S. Gao, J. Hu, Q. Liu and X. Sun, A-Site Perovskite Oxides: An Emerging Functional Material for Electrocatalysis and Photocatalysis, *J. Mater. Chem. A*, 2021, **9**(11), 6650–6670, DOI: **10.1039/D0TA09756J**.

37 C. Ma and Y. Zhang, Spinel CuxCo1−xMn2O4 Electrode for Effectively Cleaning Organic Wastewater via Electrocatalytic Oxidation, *Sep. Purif. Technol.*, 2021, **258**, 118024, DOI: **10.1016/j.seppur.2020.118024**.

38 S. Kawrani, A. A. Nada, M. F. Bekheet, M. Boulos, R. Viter, S. Roualdes, P. Miele, D. Cornu and M. Bechelany, Enhancement of Calcium Copper Titanium Oxide Photoelectrochemical Performance Using Boron Nitride Nanosheets, *Chem. Eng. J.*, 2020, **389**, 124326, DOI: **10.1016/j.cej.2020.124326**.

39 S. Kawrani, M. Boulos, D. Cornu and M. Bechelany, From Synthesis to Applications: Copper Calcium Titanate (CCTO)

and Its Magnetic and Photocatalytic Properties, *ChemistryOpen*, 2019, **8**(7), 922–950, DOI: **10.1002/open.201900133**.

40 S. Kawrani, M. Boulos, M. F. Bekheet, R. Viter, A. A. Nada, W. Riedel, S. Roualdes, D. Cornu and M. Bechelany, Segregation of Copper Oxide on Calcium Copper Titanate Surface Induced by Graphene Oxide for Water Splitting Applications, *Appl. Surf. Sci.*, 2020, **516**, 146051, DOI: **10.1016/j.apsusc.2020.146051**.

41 H. S. Kushwaha, A. Halder, P. Thomas and R. Vaish, CaCu3Ti4O12: A Bifunctional Perovskite Electrocatalyst for Oxygen Evolution and Reduction Reaction in Alkaline Medium, *Electrochim. Acta*, 2017, **252**, 532–540, DOI: **10.1016/j.electacta.2017.09.030**.

42 F. M. Praxedes, H. Moreno, A. Z. Simões, V. C. Teixeira, R. S. Nunes, R. A. C. Amoresi and M. A. Ramirez, Interface Matters: Design of an Efficient CaCu3Ti4O12-RGO Photocatalyst, *Powder Technol.*, 2022, **404**, 117478, DOI: **10.1016/j.powtec.2022.117478**.

43 J. M. Dangwang Dikdim, Y. Gong, G. B. Noumi, J. M. Sieliechi, X. Zhao, N. Ma, M. Yang and J. B. Tchatchueng, Peroxymonosulfate Improved Photocatalytic Degradation of Atrazine by Activated Carbon/Graphitic Carbon Nitride Composite under Visible Light Irradiation, *Chemosphere*, 2019, **217**, 833–842, DOI: **10.1016/j.chemosphere.2018.10.177**.

44 X. Duan, S. Yang, S. Wacławek, G. Fang, R. Xiao and D. D. Dionysiou, Limitations and Prospects of Sulfate-Radical Based Advanced Oxidation Processes, *J. Environ. Chem. Eng.*, 2020, **8**(4), 103849, DOI: **10.1016/j.jece.2020.103849**.

45 X. Zheng, X. Niu, D. Zhang, M. Lv, X. Ye, J. Ma, Z. Lin and M. Fu, Metal-Based Catalysts for Persulfate and Peroxymonosulfate Activation in Heterogeneous Ways: A Review, *Chem. Eng. J.*, 2022, **429**, 132323, DOI: **10.1016/j.cej.2021.132323**.

46 Y. Zhu, T. Wang, W. Wang, S. Chen, E. Lichtfouse, C. Cheng, J. Zhao, Y. Li and C. Wang, CaCu3Ti4O12, an Efficient Catalyst for Ibuprofen Removal by Activation of Peroxymonosulfate under Visible-Light Irradiation, *Environ. Chem. Lett.*, 2019, **17**(1), 481–486, DOI: **10.1007/s10311-018-0776-x**.

47 L. Wang, H. Xu, N. Jiang, Z. Wang, J. Jiang and T. Zhang, Trace Cupric Species Triggered Decomposition of Peroxymonosulfate and Degradation of Organic Pollutants: Cu(III) Being the Primary and Selective Intermediate Oxidant, *Environ. Sci. Technol.*, 2020, **54**(7), 4686–4694, DOI: **10.1021/acs.est.0c00284**.

48 Y. Akhi, M. Irani and M. E. Olya, Simultaneous Degradation of Phenol and Paracetamol Using Carbon/MWCNT/Fe3O4 Composite Nanofibers during Photo-like-Fenton Process, *J. Taiwan Inst. Chem. Eng.*, 2016, **63**, 327–335, DOI: **10.1016/j.jtice.2016.03.028**.

49 S. Wang, S. Gao, J. Tian, Q. Wang, T. Wang, X. Hao and F. Cui, A Stable and Easily Prepared Copper Oxide Catalyst for Degradation of Organic Pollutants by Peroxymonosulfate Activation, *J. Hazard. Mater.*, 2020, **387**, 121995, DOI: **10.1016/j.jhazmat.2019.121995**.

50 G. Li, Z. Zhong, C. Yang, Q. He and G. Peng, Degradation of Acid Orange 7 by Peroxymonosulfate Activated by Cupric Oxide, *J. Water Supply: Res. Technol.–AQUA*, 2019, **68**(1), 29–38, DOI: **10.2166/aqua.2018.096**.

51 C. Bai, G. Yang, S. Zhang, S. Deng, Y. Zhang, C. Chen, J. He, M. Xu and L. Long, A Synergistic System of Electrocatalytic-Anode/α-MnO2/Peroxymonosulfate for Removing Combined Pollution of Tetracycline and Cr(VI), *Chem. Eng. J.*, 2021, **423**, 130284, DOI: **10.1016/j.cej.2021.130284**.

52 S. Sayegh, M. Abid, F. Tanos, M. Cretin, G. Lesage, F. Zaviska, E. Petit, B. Navarra, I. Iatsunskyi, E. Coy, R. Viter, V. Fedorenko, A. Ramanavicius, A. Razzouk, J. Stephan and M. Bechelany, N-Doped TiO2 Nanotubes Synthesized by Atomic Layer Deposition for Acetaminophen Degradation, *Colloids Surf., A*, 2022, **655**, 130213, DOI: **10.1016/j.colsurfa.2022.130213**.

53 M. Hosseini, A. Esrafili, M. Farzadkia, M. Kermani and M. Gholami, Degradation of Ciprofloxacin Antibiotic Using Photo-Electrocatalyst Process of Ni-Doped ZnO Deposited by RF Sputtering on FTO as an Anode Electrode from Aquatic Environments: Synthesis, Kinetics, and Ecotoxicity Study, *Microchem. J.*, 2020, **154**, 104663, DOI: **10.1016/j.microc.2020.104663**.

54 B. O. Orimolade, B. N. Zwane, B. A. Koiki, M. Rivallin, M. Bechelany, N. Mabuba, G. Lesage, M. Cretin and O. A. Arotiba, Coupling Cathodic Electro-Fenton with Anodic Photo-Electrochemical Oxidation: A Feasibility Study on the Mineralization of Paracetamol, *J. Environ. Chem. Eng.*, 2020, **8**(5), 104394, DOI: **10.1016/j.jece.2020.104394**.

55 T. X. H. Le, T. V. Nguyen, Z. A. Yacouba, L. Zoungrana, F. Avril, E. Petit, J. Mendret, V. Bonniol, M. Bechelany, S. Lacour, G. Lesage and M. Cretin, Toxicity Removal Assessments Related to Degradation Pathways of Azo Dyes: Toward an Optimization of Electro-Fenton Treatment, *Chemosphere*, 2016, **161**, 308–318, DOI: **10.1016/j.chemosphere.2016.06.108**.

56 A. A. Nada, B. O. Orimolade, H. H. El-Maghrabi, B. A. Koiki, M. Rivallin, M. F. Bekheet, R. Viter, D. Damberga, G. Lesage, I. Iatsunskyi, E. Coy, M. Cretin, O. A. Arotiba and M. Bechelany, Photoelectrocatalysis of Paracetamol on Pd–ZnO/N-Doped Carbon Nanofibers Electrode, *Appl. Mater. Today*, 2021, **24**, 101129, DOI: **10.1016/j.apmt.2021.101129**.

57 J. Li, M. A. Subramanian, H. D. Rosenfeld, C. Y. Jones, B. H. Toby and A. W. Sleight, Clues to the Giant Dielectric Constant of $CaCu_3Ti_4O_{12}$ in the Defect Structure of "$SrCu_3Ti_4O_{12}$", *Chem. Mater.*, 2004, **16**(25), 5223–5225, DOI: **10.1021/cm048345u**.

58 N. Hoang Nam, Raman Spectroscopy of CaCu3Ti4O12 Ceramics Revisited, *VNU Journal of Science: Mathematics–Physics*, 2018, **34**(3), 79–84, DOI: **10.25073/2588-1124/vnumap.4289**.

59 M. Balık, V. Bulut and I. Y. Erdogan, Optical, Structural and Phase Transition Properties of Cu2O, CuO and Cu2O/CuO: Their Photoelectrochemical Sensor Applications, *Int. J. Hydrogen Energy*, 2019, **44**(34), 18744–18755, DOI: **10.1016/j.ijhydene.2018.08.159**.

60 S. Park, H. Kwon, D. Park, H. Cheong and G. Park, Origin of ferroelectric-like hysteresis loop of CaCu3Ti4O12 ceramic studied by impedance and micro-Raman spectroscopy, *arXiv*,

2011, preprint, arXiv:1109.2959, DOI: 10.48550/arXiv.1109.2959.

61 F. Wu, Y. Myung and P. Banerjee, Unravelling Transient Phases during Thermal Oxidation of Copper for Dense CuO Nanowire Growth, *CrystEngComm*, 2014, **16**(16), 3264–3267, DOI: 10.1039/C4CE00275J.

62 S. Maity, M. Samanta, A. Sen and K. K. Chattopadhyay, Investigation of Electrochemical Performances of Ceramic Oxide CaCu3Ti4O12 Nanostructures, *J. Solid State Chem.*, 2019, **269**, 600–607, DOI: 10.1016/j.jssc.2018.10.016.

63 L.-T. Mei, H.-I. Hsiang and T.-T. Fang, Effect of Copper-Rich Secondary Phase at the Grain Boundaries on the Varistor Properties of $CaCu_3Ti_4O_{12}$ Ceramics, *J. Am. Ceram. Soc.*, 2008, **91**(11), 3735–3737, DOI: 10.1111/j.1551-2916.2008.02674.x.

64 W. Hao, J. Zhang, Y. Tan and W. Su, Giant Dielectric-Permittivity Phenomena of Compositionally and Structurally $CaCu_3Ti_4O_{12}$ -Like Oxide Ceramics, *J. Am. Ceram. Soc.*, 2009, **92**(12), 2937–2943, DOI: 10.1111/j.1551-2916.2009.03298.x.

65 P. R. Bueno, R. Tararan, R. Parra, E. Joanni, M. A. Ramírez, W. C. Ribeiro, E. Longo and J. A. Varela, A Polaronic Stacking Fault Defect Model for $CaCu_3Ti_4O_{12}$ Material: An Approach for the Origin of the Huge Dielectric Constant and Semiconducting Coexistent Features, *J. Phys. D: Appl. Phys.*, 2009, **42**(5), 055404, DOI: 10.1088/0022-3727/42/5/055404.

66 M. Grao, J. Redfern, P. J. Kelly and M. Ratova, Magnetron Co-Sputtered Bi12TiO20/Bi4Ti3O12 Composite – An Efficient Photocatalytic Material with Photoinduced Oxygen Vacancies for Water Treatment Application, *Appl. Surf. Sci.*, 2021, **552**, 149486, DOI: 10.1016/j.apsusc.2021.149486.

67 H. Moreno, M. Damm, S. M. Freitas, M. V. S. Rezende, A. Z. Simões, G. Biasotto, V. R. Mastelaro, V. C. Teixeira and M. A. Ramirez, Unveiling Photoluminescent Response of Ce-Doped CaCu3Ti4O12: An Experimental-Theoretical Approach, *J. Alloys Compd.*, 2022, **923**, 166185, DOI: 10.1016/j.jallcom.2022.166185.

68 P. Y. Raval, P. R. Pansara, N. H. Vasoya, K. Punia, S. N. Dolia, K. B. Modi and S. Kumar, First Observation of Reversible Mechanochromism and Chromaticity Study on Calcium–Copper–Titanate, *J. Am. Ceram. Soc.*, 2019, **102**(11), 6872–6881, DOI: 10.1111/jace.16609.

69 S. Orrego, J. A. Cortés, R. A. C. Amoresi, A. Z. Simões and M. A. Ramírez, Photoluminescence Behavior on Sr 2+ Modified CaCu 3 Ti 4 O 12 Based Ceramics, *Ceram. Int.*, 2018, **44**(9), 10781–10789, DOI: 10.1016/j.ceramint.2018.03.116.

70 A. A. Felix, M. Spreitzer, D. Vengust, D. Suvorov and M. O. Orlandi, Probing the Effects of Oxygen-Related Defects on the Optical and Luminescence Properties in CaCu3Ti4O12 Ceramics, *J. Eur. Ceram. Soc.*, 2018, **38**(15), 5002–5006, DOI: 10.1016/j.jeurceramsoc.2018.06.045.

71 M. A. Pires, C. Israel, W. Iwamoto, R. R. Urbano, O. Agüero, I. Torriani, C. Rettori, P. G. Pagliuso, L. Walmsley, Z. Le, J. L. Cohn and S. B. Oseroff, Role of Oxygen Vacancies in the Magnetic and Dielectric Properties of the High-Dielectric-Constant System CaCu 3 Ti 4 O 12: An Electron-Spin Resonance Study, *Phys. Rev. B: Condens. Matter Mater. Phys.*, 2006, **73**(22), 224404, DOI: 10.1103/PhysRevB.73.224404.

72 Y. Deng, A. D. Handoko, Y. Du, S. Xi and B. S. Yeo, In Situ Raman Spectroscopy of Copper and Copper Oxide Surfaces during Electrochemical Oxygen Evolution Reaction: Identification of Cu^{III} Oxides as Catalytically Active Species, *ACS Catal.*, 2016, **6**(4), 2473–2481, DOI: 10.1021/acscatal.6b00205.

73 X. Miao, L. Wu, Y. Lin, X. Yuan, J. Zhao, W. Yan, S. Zhou and L. Shi, The Role of Oxygen Vacancies in Water Oxidation for Perovskite Cobalt Oxide Electrocatalysts: Are More Better?, *Chem. Commun.*, 2019, **55**(10), 1442–1445, DOI: 10.1039/C8CC08817A.

74 J. Kim, X. Yin, K.-C. Tsao, S. Fang and H. Yang, $Ca_2Mn_2O_5$ as Oxygen-Deficient Perovskite Electrocatalyst for Oxygen Evolution Reaction, *J. Am. Chem. Soc.*, 2014, **136**(42), 14646–14649, DOI: 10.1021/ja506254g.

75 T. ul Haq and Y. Haik, S Doped Cu2O-CuO Nanoneedles Array: Free Standing Oxygen Evolution Electrode with High Efficiency and Corrosion Resistance for Seawater Splitting, *Catal. Today*, 2022, **400–401**, 14–25, DOI: 10.1016/j.cattod.2021.09.015.

76 J. R. Petrie, H. Jeen, S. C. Barron, T. L. Meyer and H. N. Lee, Enhancing Perovskite Electrocatalysis through Strain Tuning of the Oxygen Deficiency, *J. Am. Chem. Soc.*, 2016, **138**(23), 7252–7255, DOI: 10.1021/jacs.6b03520.

77 Y. Chen, H. Hu, X. Jiao, M. Du, B. Wang and Y. Zhang, Enhanced Electrochemical Oxidation of Oxytetracycline on Oxygen Vacancy-Rich MnO@N-Doped C Anode: Transformation Pathway and Toxicity Assessment, *Sep. Purif. Technol.*, 2023, **305**, 122438, DOI: 10.1016/j.seppur.2022.122438.

78 Y. Zhang, M. Gan, L. Ma, W. Zhao, X. Li, X. Hua and L. Wang, Oxygen Vacancy-Enriched Co_3O_4 as Efficient Co-catalyst for Pt Nanoparticles towards Methanol Electrooxidation, *ChemElectroChem*, 2022, **9**(4), e202101516, DOI: 10.1002/celc.202101516.

79 L. Wang, H. Xu, N. Jiang, Z. Wang, J. Jiang and T. Zhang, Trace Cupric Species Triggered Decomposition of Peroxymonosulfate and Degradation of Organic Pollutants: Cu(III) Being the Primary and Selective Intermediate Oxidant, *Environ. Sci. Technol.*, 2020, **54**(7), 4686–4694, DOI: 10.1021/acs.est.0c00284.

80 Y. Ding, L. Fu, X. Peng, M. Lei, C. Wang and J. Jiang, Copper Catalysts for Radical and Nonradical Persulfate Based Advanced Oxidation Processes: Certainties and Uncertainties, *Chem. Eng. J.*, 2022, **427**, 131776, DOI: 10.1016/j.cej.2021.131776.

81 J. Wang and S. Wang, Reactive Species in Advanced Oxidation Processes: Formation, Identification and Reaction Mechanism, *Chem. Eng. J.*, 2020, **401**, 126158, DOI: 10.1016/j.cej.2020.126158.

82 Y. Huang, J. Li, P. Du and X. Lu, Rational Design of Copper Encapsulated within Nitrogen-Doped Carbon Core-Shell

Nanosphere for Efficiently Photocatalytic Peroxymonosulfate Activation, *J. Colloid Interface Sci.*, 2021, **597**, 206–214, DOI: **10.1016/j.jcis.2021.04.016**.

83 Q. Zhang, X. Sun, Y. Dang, J.-J. Zhu, Y. Zhao, X. Xu and Y. Zhou, A Novel Electrochemically Enhanced Homogeneous PMS-Heterogeneous CoFe2O4 Synergistic Catalysis for the Efficient Removal of Levofloxacin, *J. Hazard. Mater.*, 2022, **424**, 127651, DOI: **10.1016/j.jhazmat.2021.127651**.

84 P. Liang, D. Meng, Y. Liang, Z. Wang, C. Zhang, S. Wang and Z. Zhang, Cation Deficiency Tuned LaCoO3−δ Perovskite for Peroxymonosulfate Activation towards Bisphenol A Degradation, *Chem. Eng. J.*, 2021, **409**, 128196, DOI: **10.1016/j.cej.2020.128196**.

85 M. D. G. de Luna, M. L. Veciana, C.-C. Su and M.-C. Lu, Acetaminophen Degradation by Electro-Fenton and Photoelectro-Fenton Using a Double Cathode Electrochemical Cell, *J. Hazard. Mater.*, 2012, **217–218**, 200–207, DOI: **10.1016/j.jhazmat.2012.03.018**.

86 K. Wang, G. Liang, M. Waqas, B. Yang, K. Xiao, C. Zhu and J. Zhang, Peroxymonosulfate Enhanced Photoelectrocatalytic Degradation of Ofloxacin Using an Easily Coated Cathode, *Sep. Purif. Technol.*, 2020, **236**, 116301, DOI: **10.1016/j.seppur.2019.116301**.

87 T. X. Huong Le, M. Drobek, M. Bechelany, J. Motuzas, A. Julbe and M. Cretin, Application of Fe-MFI Zeolite Catalyst in Heterogeneous Electro-Fenton Process for Water Pollutants Abatement, *Microporous Mesoporous Mater.*, 2019, **278**, 64–69, DOI: **10.1016/j.micromeso.2018.11.021**.

88 S. O. Ganiyu, T. X. Huong Le, M. Bechelany, N. Oturan, S. Papirio, G. Esposito, E. van Hullebusch, M. Cretin and M. A. Oturan, Electrochemical Mineralization of Sulfamethoxazole over Wide PH Range Using FeIIFeIII LDH Modified Carbon Felt Cathode: Degradation Pathway, Toxicity and Reusability of the Modified Cathode, *Chem. Eng. J.*, 2018, **350**, 844–855, DOI: **10.1016/j.cej.2018.04.141**.

89 S. Liang, H. Lin, X. Yan and Q. Huang, Electro-Oxidation of Tetracycline by a Magnéli Phase Ti4O7 Porous Anode: Kinetics, Products, and Toxicity, *Chem. Eng. J.*, 2018, **332**, 628–636, DOI: **10.1016/j.cej.2017.09.109**.

90 H. Olvera-Vargas, J.-C. Rouch, C. Coetsier, M. Cretin and C. Causserand, Dynamic Cross-Flow Electro-Fenton Process Coupled to Anodic Oxidation for Wastewater Treatment: Application to the Degradation of Acetaminophen, *Sep. Purif. Technol.*, 2018, **203**, 143–151, DOI: **10.1016/j.seppur.2018.03.063**.

91 J. Wang and S. Wang, Toxicity Changes of Wastewater during Various Advanced Oxidation Processes Treatment: An Overview, *J. Cleaner Prod.*, 2021, **315**, 128202, DOI: **10.1016/j.jclepro.2021.128202**.

92 G. Dong, K. Lang, Y. Gao, W. Zhang, D. Guo, J. Li, D.-F. Chai, L. Jing, Z. Zhang and Y. Wang, A Novel Composite Anode via Immobilizing of Ce-Doped PbO2 on CoTiO3 for Efficiently Electrocatalytic Degradation of Dye, *J. Colloid Interface Sci.*, 2022, **608**, 2921–2931, DOI: **10.1016/j.jcis.2021.11.023**.

93 L. Chen, Y. Zhang and C. Ma, Perovskites SrxLa1-XMnyCo1-YO3-δ Coated on Ti as Stable Non-Noble Anode for Efficient Electrocatalytic Oxidation of Organic Wastewater Containing Ammonia Nitrogen, *Chem. Eng. J.*, 2020, **393**, 124514, DOI: **10.1016/j.cej.2020.124514**.

94 O. V. Nkwachukwu, C. Muzenda, B. A. Koiki and O. A. Arotiba, Perovskites in Photoelectrocatalytic Water Treatment: Bismuth Ferrite - Graphite Nanoparticles Composite Photoanode for the Removal of Ciprofloxacin in Water, *J. Photochem. Photobiol., A*, 2023, **434**, 114275, DOI: **10.1016/j.jphotochem.2022.114275**.